

HIGH-RESOLUTION X-RAY SPECTROSCOPY OF THE INTERSTELLAR MEDIUM: STRUCTURE AT THE OXYGEN ABSORPTION EDGE

ADRIENNE M. JUETT¹, NORBERT S. SCHULZ, AND DEEPTO CHAKRABARTY^{1,2}
 Center for Space Research, Massachusetts Institute of Technology, Cambridge, MA 02139;
 ajuett, nss, deepto@space.mit.edu

To be published in the Astrophysical Journal, vol 612

ABSTRACT

We present high-resolution spectroscopy of the oxygen K -shell interstellar absorption edge in seven X-ray binaries using the High Energy Transmission Grating Spectrometer (HETGS) onboard the *Chandra X-ray Observatory*. Using the brightest sources as templates, we found a best-fit model of two absorption edges and five Gaussian absorption lines. All of these features can be explained by the recent predictions of K -shell absorption from neutral and ionized atomic oxygen. We identify the $K\alpha$ and $K\beta$ absorption lines from neutral oxygen, as well as the $S = 3/2$ absorption edge. The expected $S = 1/2$ edge is not detected in these data due to overlap with instrumental features. We also identify the $K\alpha$ absorption lines from singly and doubly ionized oxygen. The O I $K\alpha$ absorption line is used as a benchmark with which to adjust the absolute wavelength scale for theoretical predictions of the absorption cross-sections. We find that shifts of 30–50 mÅ are required, consistent with differences previously noticed from comparisons of the theory with laboratory measurements. Significant oxygen features from dust or molecular components, as suggested in previous studies, are not required by our HETGS spectra. With these spectra, we can begin to measure the large-scale properties of the interstellar medium (ISM). We place a limit on the velocity dispersion of the neutral lines of $\lesssim 200$ km s^{−1}, consistent with measurements at other wavelengths. We also make the first measurement of the oxygen ionization fractions in the ISM. We constrain the interstellar ratio of O II/O I to ≈ 0.1 and the ratio of O III/O I to $\lesssim 0.1$. This work demonstrates the utility of X-ray spectroscopy for studies of the ISM. Future work will provide measurements of the relative abundances and ionization fractions for elements from carbon to iron.

Subject headings: ISM: general — X-rays: ISM — X-rays: binaries

1. INTRODUCTION

In the space between the stars resides the interstellar medium (ISM), composed of gas and dust and containing both compact clouds and a diffuse component. The diffuse ISM has four major phases: cold neutral, warm neutral, warm ionized, and hot ionized (Heiles & Kulkarni 1987). Despite years of study, questions still remain as to the relationship between these components. High-resolution X-ray observations from the *Chandra X-ray Observatory* and *XMM-Newton* offer a new window with which to study the ISM.

The ISM affects X-ray spectra in two ways: photoelectric absorption, particularly at low energies, and scattering by dust grains, producing X-ray halos. At X-ray energies, absorption features are from the excitation and ionization of inner-shell (K -shell) electrons, although for high- Z elements like iron, L -shell absorption edges are also detectable. The wavelength range available to *Chandra* and *XMM* includes absorption features from carbon through iron. Since the abundances of these elements are substantially lower than for hydrogen and helium, X-ray studies can probe the ISM over larger distances than is possible in the optical and ultraviolet. Measurements of the ISM absorption features in the spectra of X-ray binaries will allow us to study the abundances and ionization fractions for a large number of elements. This study is analogous to optical and ultraviolet observations of stars

and quasars that measure ISM and intergalactic medium absorption features. X-ray binaries are the brightest objects in the X-ray sky and therefore require only moderate observation lengths to produce high signal-to-noise spectra.

An understanding of the ISM absorption features is also important for determining the intrinsic spectral properties of X-ray sources. Early photoelectric absorption models assumed that the ISM was composed of a neutral, monoatomic, homogeneous gas with solar abundances (see e.g., Brown & Gould 1970). Ride & Walker (1977) were the first to compute a more complex 2-phase photoelectric absorption model which more closely resembles the actual ISM. Improvements in X-ray absorption cross-sections, and solar and ISM abundance data, led to updated absorption models (Morrison & McCammon 1983; Balucińska-Church & McCammon 1992; Wilms, Allen, & McCray 2000).

While the recent models provide good fits to low- and medium-resolution X-ray spectra, they are not appropriate for the grating spectra available with *Chandra* and *XMM*. Most importantly, the absorption cross-sections utilized in the standard models (Henke, Gullikson, & Davis 1993; Verner et al. 1993; Verner & Yakovlev 1995) do not accurately describe the resonance structure of the edges. Instead, the cross-sections are modeled by a step function at a fixed edge position. The positions were determined either from low-resolution solid-state data (Henke et al.

¹ Also Department of Physics, Massachusetts Institute of Technology, Cambridge, MA 02139

² Alfred P. Sloan Research Fellow

1993) or from theoretical calculations (Verner et al. 1993; Verner & Yakovlev 1995), neither of which can be reliably taken as the true atomic edge position. Additionally, the models do not include any contribution from ionized forms of the elements. The limitations of the standard absorption models are well known (see Wilms et al. 2000), yet no high-resolution model is available for standard usage.

The first attempt to measure ISM absorption edges in the X-rays used the *Einstein* Focal Plane Crystal Spectrometer (Schattenburg & Canizares 1986) and found evidence for the O I $1s$ - $2p$ ($K\alpha$) absorption resonance and a possible O II edge. Recent *Chandra* and *XMM* results have revealed more complex structure around the oxygen K -shell absorption edge. Three studies have used *Chandra* to study ISM absorption edges in X-ray binary spectra (Paerels et al. 2001; Schulz et al. 2002; Takei et al. 2002). Each found a prominent O I $1s$ - $2p$ resonance absorption line at 23.51 Å and evidence for another line feature at ≈ 23.36 Å, attributed to compound forms of oxygen, but also consistent with the O II $1s$ - $2p$ transition. Takei et al. (2002) found that the oxygen edge in Cyg X-2 could be best fit by a model consisting of three absorption edges, representing the two edges in atomic oxygen absorption and a contribution from oxygen in molecular forms. Using the *XMM* Reflection Grating Spectrometer, de Vries et al. (2003) found that the ISM oxygen K -shell edge of both X-ray binaries and extragalactic sources was well described by the theoretical R-matrix calculation of atomic oxygen (McLaughlin & Kirby 1998), although requiring a shift of the edge complex relative to the $1s$ - $2p$ transition. All of the high-resolution work points to a complex system of absorption features at the oxygen edge, not the simple step function used in absorption models.

The purpose of this work is to compile a large sample of spectra to study the oxygen K -shell edge complex. Other ISM edges will be studied in a future work. One of our goals is to provide the community with a reasonable model for the oxygen K -shell edge complex for use in future analyses. The high-resolution astrophysical data can also be used to test our understanding of the atomic structure that leads to features in photoelectric absorption by comparing with theoretical calculations. Finally, we will study the nature of the ISM by measuring the abundances in various ionizations states and studying the uniformity of the ISM absorption. Combined with similar studies of other edges, high-resolution X-ray spectra will in the future probe relative abundances and depletion in the ISM.

2. EXPECTED STRUCTURE OF THE OXYGEN ABSORPTION EDGE

The interstellar absorption features found in the X-ray band are due to ionization of inner-shell ($n = 1$) electrons in neutral atoms. This absorption results in a series of absorption edge complexes, one for each element. The cross-section for each edge has a similar large-scale energy dependence. Photons with energies below the ionization potential cannot ionize the atom, and the cross-section is negligible. At the ionization energy, the cross-section is large and then decreases roughly as $E^{-2.7}$ at higher energies. The reduction at higher energies is due to the increasing probability that a photon has enough

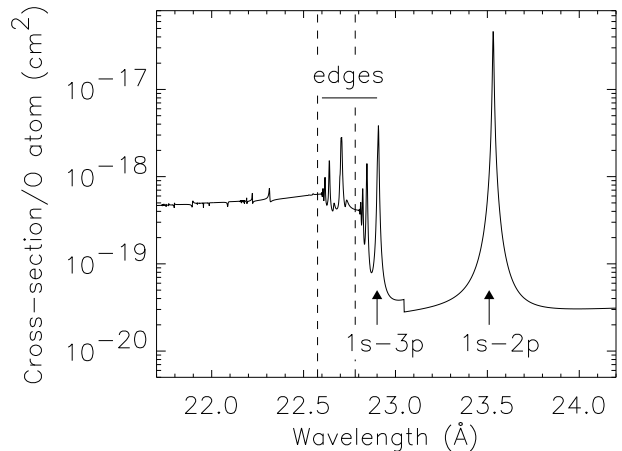


FIG. 1.— Calculated theoretical cross-section of neutral oxygen, from Gorczyca & McLaughlin (2000). Labeled are the positions of the $1s$ - $2p$ and $1s$ - $3p$ transitions and the edges. The dotted lines show the positions of the $S = 3/2$ and $S = 1/2$ resonance series limits at 22.781 and 22.576 Å, respectively.

energy that it just passes by the atom without ionizing it. This description is employed in the standard absorption models and is reasonable for CCD-resolution spectra.

But with the higher-resolution spectra available from grating instruments, we can resolve finer structure. The most important effect is due to excitation of a K -shell electron into a higher orbital. Photons with energy slightly less (or wavelengths greater) than the ionization energy can excite the electron into a higher n shell. This produces narrow absorption lines at the excitation energies yielding the $1s$ - $2p$ ($K\alpha$), $1s$ - $3p$ ($K\beta$), etc., features. The $1s$ - np series of lines is termed a resonance series, ending at the series limit or ionization energy ($n \rightarrow \infty$). More structure in the edge results from considering the spin of the final state of the atom. For oxygen, the ionized O^+ product with a $1s$ hole can have total spin angular momentum $S = 1/2$ or $S = 3/2$, producing separate series limits at different energies due to the spin-dependent exchange force. Each series limit has an associated resonance series from neutral oxygen excitations which have the same configuration of the inner shells ($n = 1, 2$ with a $1s$ hole), neglecting the contribution of the valence ($n \geq 3$) electron. In addition, differences in the total orbital angular momentum L of the final state also give rise to different resonance series. The dominant final states have $L = 1$ with $S = 1/2$ and $S = 3/2$, the configurations $1s2s^22p^4(^2P)$ and $1s2s^22p^4(^4P)$, respectively. There are also additional series associated with the $L = 0$ and $L = 2$ final states, $1s2s^22p^4(^2S)$ and $1s2s^22p^4(^2D)$, respectively (see McLaughlin & Kirby 1998), but these will produce weaker features since they require both a promotion of a $1s$ - np electron and a transition in the $2p^4$ subshell. These weaker features are undetectable with current X-ray observatories.

To calculate the theoretical photoelectric absorption cross-sections, one must solve the Schrödinger equation. For atoms with only one electron (hydrogen-like) this calculation is straightforward and exactly solvable, but as

TABLE 1. THEORETICAL PREDICTIONS FOR OXYGEN *K* EDGE FEATURES

Feature	Predicted λ (Å)	Shifted λ (Å)
Gorczyca & McLaughlin 2000		
1s-2p	23.532	23.508 ^a
1s-3p	22.907	22.884
1s2s ² 2p ⁴ (⁴ P)	22.781	22.758
1s2s ² 2p ⁴ (² P)	22.576	22.553
Pradhan et al. 2003		
O I 1s-2p	23.45	23.508 ^a
O II 1s-2p	23.27	23.33
O III 1s-2p	23.08	23.14
	23.02	23.08
	22.93	22.99
O IV 1s-2p	22.73	22.79
	22.67	22.73
	22.46	22.52

^aReferenced to weighted mean of observational results, see § 5.

the number of electrons in the atom increases, so does the complexity of the calculation. Multi-electron atoms require numerical methods to solve for the cross-sections. Such methods are only able to approximate the solution of the Schrödinger equation. There are a number of numerical techniques employed (see Bautista 2000, for a review). The preferred method for calculating cross-sections that include resonance structure is the R-matrix method. While the structure and strength of the cross-sections calculated using the R-matrix method compare well with laboratory measurements, the absolute positions are different. This results from the truncation of the wavefunction description of the resulting ion, which is necessary to keep the computation manageable. In practice, the energies of the theoretical cross-sections are shifted when compared to laboratory data.

Motivated by the high-resolution spectroscopy possible with *Chandra* and *XMM*, several groups have published theoretical calculations of the cross-sections of inner-shell processes in atomic and ionized oxygen (McLaughlin & Kirby 1998; Gorczyca & McLaughlin 2000; Pradhan et al. 2003). As mentioned above, the cross-section of atomic oxygen in the vicinity of the *K* edge is dominated by two resonance series converging to the limits corresponding to the ²P and ⁴P states of O⁺ (see e.g., McLaughlin & Kirby 1998). Laboratory data (Menzel et al. 1996; Stolte et al. 1997; McLaughlin & Kirby 1998) compare well qualitatively to these calculations, but discrepancies in the positions of the resonance features were noted by both Stolte et al. (1997) and McLaughlin & Kirby (1998). More recent work (Gorczyca & McLaughlin 2000) has improved on the theoretical calculations in order to better match the data. Gorczyca & McLaughlin (2000) adjusted their theoretical calculation to match the threshold energies found by Stolte et al. (1997), producing theoretical data that matches laboratory measurements well in both cross-section and position of the resonance features. It should be noted that while laboratory measurements have very good relative accuracy, the absolute positional accuracy is less well known. We therefore find it reasonable to suggest that the energy scale of the laboratory measurements, and consequently the theoretical calculations, may require a shift to match the wavelength cal-

ibration of the *Chandra* data. Figure 1 shows the calculated cross-section of Gorczyca & McLaughlin (2000) along with identified features. Table 1 lists the predicted wavelengths of the important resonance features, i.e. the 1s-2p and 1s-3p resonance lines, and the two series limits as found by Gorczyca & McLaughlin (2000), as well as the expected values of those features when the 1s-2p transition is shifted to the mean value found in our analysis (see §5).

Along with neutral oxygen, we would expect ionized oxygen to be present in the ISM. Pradhan et al. (2003) calculated the positions and cross-sections of the 1s-2p resonance features from all ionized forms of oxygen. Table 1 lists the predicted wavelengths of the O I–O IV lines, as well as their positions when the O I 1s-2p position is shifted to the mean value found in our analysis (see §5). The Pradhan et al. (2003) result shows a significant discrepancy with the Gorczyca & McLaughlin (2000) result for the predicted wavelength of the O I 1s-2p transition. While the absolute positions may differ due to differences in the calculation, we assume that the relative positions of these features are reliable. We can test this assumption by comparing the theoretical position of the O II line to the laboratory measurement of 23.35 Å (Kawatsura et al. 2002). The position given by Pradhan et al. (2003) is 23.27 Å, but when our shift is applied, the theoretical position becomes 23.33 Å, in much better agreement with the laboratory measurement. We have recently become aware of new calculations of the full *K*-shell absorption edge cross-sections for ionized oxygen (Gorczyca 2004, in prep.), but do not include these results in our analysis.

3. OBSERVATIONS AND THE HETGS OXYGEN EDGE

Our study is based on archival observations of seven bright X-ray binaries obtained with *Chandra* using the High Energy Transmission Grating Spectrometer (HETGS) in combination with the Advanced CCD Imaging Spectrometer (ACIS; Weisskopf et al. 2002). The HETGS spectra are imaged by ACIS, an array of six CCD detectors. The HETGS/ACIS combination provides both an undispersed (zeroth order) image and dispersed spectra from the gratings. The various orders overlap and are sorted using the intrinsic energy resolution of the ACIS CCDs. The HETGS carries two transmission gratings: the Medium Energy Gratings (MEGs) with a range of 2.5–31 Å (0.4–5.0 keV) and the High Energy Gratings (HEGs) with a range of 1.2–15 Å (0.8–10.0 keV). The first-order MEG (HEG) spectrum has a spectral resolution of $\Delta\lambda = 0.023$ Å (0.012 Å).

Of the previous ISM studies of the oxygen *K*-shell edge, only one (Schulz et al. 2002) was performed with the HETGS. The oxygen edge is accessible with the HETGS exclusively via the MEG. The other studies were performed with either the Low Energy Transmission Grating Spectrometer (LETGS) on *Chandra*, or the Reflection Grating Spectrometer (RGS) on *XMM*. The MEG offers the highest available spectral resolution $\lambda/\Delta\lambda \approx 1000$, compared with 460 for the LETGS, and 300 for the RGS at 23 Å, but the lowest effective area (5, 8, and 60 cm² for the MEG, LETGS, and RGS respectively at 23 Å).

The MEG images both the positive and negative grating orders onto ACIS. For the oxygen edge region of the

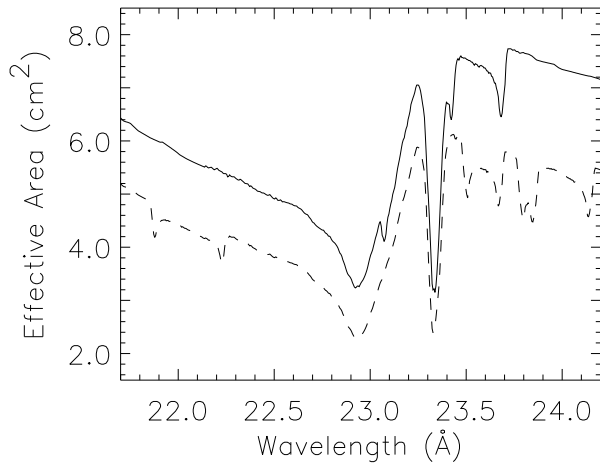


FIG. 2.— Effective area curves of the MEG -1 order spectra on ACIS-S1 for two observations. The solid line is from the Cyg X-2 observation taken 1999 September 23, while the dashed line is from the Cyg X-1 observation taken 2002 July 30 (ObsID 3724). The difference in the effective area is due to the contaminant which is building up on the ACIS detector.

spectrum, the -1 order is readout by the back-side illuminated S1 CCD, while the $+1$ order is readout by the front-side illuminated S4 CCD. In the brightest sources, we found a count excess in the $+1$ spectrum at the oxygen edge, possibly from a previously undetected hot pixel, and have therefore chosen to restrict our analysis to the -1 MEG spectrum. Since the effective area of S1 is ≈ 6 times larger than S4, this does not significantly affect our count rate. The effective area curve of the MEG -1 order is shown in Figure 2. The structure in the oxygen K -shell region is from internal absorption in the CCDs and the optical blocking filter (OBF). The feature at 23.33 \AA is likely from the $1s-2p$ resonance of double-bonded oxygen found in the OBF, which is composed of polyimide (a polycarbonate plastic). A similar resonance feature is found in absorption spectra of O_2 (A. Hitchcock, priv. comm.). The instrumental features were well determined prior to the launch of *Chandra* in 1999³ (Prigozhin et al. 1997).

Along with the known instrumental contribution to the oxygen edge, a time-dependent reduction in the effective area of ACIS has been detected at low energies. This reduction is due to a layer of contaminant that is accumulating on the ACIS detector which absorbs incoming X-rays. The contaminant gradually reduces the detector quantum efficiency with time and affects all wavelengths, particularly those above 6 \AA . The *Chandra* instrument teams have studied the spectral profile of the contaminant absorption using LETGS spectra and have modeled its structure and time-dependence (Marshall et al. 2003). An estimated correction for the contaminant is now available through the *Chandra* website⁴. The biggest effect is an overall reduction in effective area at the oxygen edge due to the large optical depth of carbon. Fig-

TABLE 2. OBSERVATION LOG

Source Name	ObsID	Observation Date	Time (ks)
Cyg X-2	1102	1999-09-23	29
Cyg X-1	107	1999-10-19	9
	3407	2001-10-28	21
	3724	2002-07-30	14
4U 1636–53	105	1999-10-20	29
	1939	2001-03-28	26
4U 1735–44	704	2000-06-09	24
GX 9+9	703	2000-08-22	21
4U 1543–624	702	2000-09-12	27
4U 1820–30	1021	2001-07-21	9
	1022	2001-09-12	9

ure 2 shows the change in the effective area over time, from 1999 September to 2002 July. In addition, a small ($\tau=0.10$ in 2002 October) oxygen edge from the contaminant is also detected. There is some discrepancy between the predicted optical depth of oxygen (based on the behavior of the carbon optical depth) and the measured oxygen optical depth, which is not understood (Marshall et al. 2003). Since all of our observations were taken before October 2002, the contaminant contribution to the oxygen optical depth is $\lesssim 0.10$ for all observations, which translates to less than 10% of the total instrumental edge. This is comparable to the uncertainty on our optical depth measurements (see §5), and therefore our results should not be significantly affected by the uncertainties in the contaminant contribution. A more important issue is the structure of the contaminant edge. High-resolution studies reveal structure similar to that of the OBF (Marshall et al. 2003). Thus, besides changes in the instrumental optical depth, the contaminant also adds to the equivalent width of the instrumental absorption feature at 23.33 \AA . It should be noted that the high-resolution structure of the oxygen edge was determined using a single observation (Marshall et al. 2003), and no estimate of the error in this measurement is available. We assume the contaminant correction is accurate, but see §6 for possible problems with the correction.

In Table 2, we list the observations used in this analysis. The data sets were reduced using the standard CIAO threads⁵. In some cases, the zeroth-order data was not telemetered. For these observations, we estimated the zeroth-order position by finding the intersection of the grating arms and readout streak. After spectral extraction, the accuracy of the estimated zeroth-order position was verified by comparing the wavelengths of strong instrumental edges in both plus and minus sides of the spectra. Events collected during thermonuclear X-ray bursts were excluded from this analysis. Since the individual observations of 4U 1820–30 and 4U 1636–53 were brief, the spectra from multiple observations were combined for each source in order to improve statistics. Detector response files (ARFs and RMFs) were created for the -1 MEG spectra. We corrected the standard CIAO ARFs for the time-dependent change in the response due to the contaminant on ACIS using the `contamarf` tool.

4. SPECTRAL FITTING PROCEDURE

³ For information on the calibration of the OBF see http://www.astro.psu.edu/xray/docs/cal_report/cal_report.html.

⁴ See <http://asc.harvard.edu/ciao/threads/aciscontam/>

⁵ <http://asc.harvard.edu/ciao/threads/>

We fit only the 21.5–24.5 Å wavelength range and binned the data to ensure at least 10 counts per bin. An absorbed power-law continuum model was used for all sources except Cyg X-1, where an absorbed disk black-body model was used. We initially allowed the continuum parameters to vary during the fits, but visual inspection revealed that the best-fit parameters underestimated the continuum level at wavelengths greater than the edge. To better estimate the continuum level, we fit the line-free region of the data between 23.7 and 24.7 Å and then fixed the continuum parameters to the measured values in subsequent fits of the oxygen edge region. We will present results from the fixed continuum fits, as well as note differences between fixed and free continuum methods as an estimate of the systematic uncertainty on our results. The `tbvarabs` absorption model (Wilms et al. 2000) was used with the oxygen abundance set to zero to allow for an explicit modeling of the oxygen absorption. The equivalent hydrogen column density (N_{H}) was fixed in all fits to a value consistent with the measured oxygen edge depth, assuming the Wilms et al. (2000) oxygen abundance.

We modeled the oxygen absorption edge by using two edge models which mimic the structure of the theoretical determination of the edge (McLaughlin & Kirby 1998; Gorczyca & McLaughlin 2000). The position of the 22.6 Å edge was always fixed. For 4U 1735–44 and 4U 1543–624, the 22.8 Å edge position was also fixed in the fits. Both edge depths were always varied, although for the lower column density sources, only upper limits on the depth of the 22.6 Å edge were obtained. We allowed the two edge depths to vary independently in order to test if both edge components are detectable as claimed by Takei et al. (2002). Since the ratio of the edge depths is a fixed quantity given by the atomic cross-section, we should find a consistent value for this ratio if both edges are detected in our data. This test allows us to understand the sensitivity of our data to the edge structure.

To determine the most appropriate model for the oxygen edge region, we used the observations of the brightest sources, Cyg X-2 and Cyg X-1 (ObsID 107) as templates (Figure 3). Our model included absorption lines for the 23.5 Å and 23.36 Å lines seen in other analyses (Paerels et al. 2001; Schulz et al. 2002; Takei et al. 2002). For most sources the widths of these lines were allowed to vary along with the line position and depth. In some cases, the widths had to be constrained to prevent unrealistically large values. The position of the 23.36 Å line in the fit of the 4U 1543–624 spectra was fixed. We also included two absorption lines in the 23.0–23.2 Å wavelength range and another at 22.8–22.9 Å. For these lines, we fixed the line width to the instrumental resolution of 0.023 Å FWHM (or a sigma of 0.01 Å), while allowing the position and depth to find the best-fit values. The best-fit parameters were then used to determine the equivalent widths (EWs) of the lines. Figures 4 and 5 show the spectra and best-fit model for all datasets. All error estimates are 90%-confidence levels, unless otherwise noted, and do not include instrumental errors. The absolute wavelength accuracy of the MEG is ± 0.011 Å FWHM.

By fitting with two edge models, we hoped to resolve the $S = 1/2$ and $S = 3/2$ series limits as seen in theoretical models. The lack of a consistent ratio between the two edges, suggests that our data are not good enough to consistently detect the $S = 1/2$ edge. Since this is true, we have developed a method to determine the column density of each edge that is independent of the model used to fit the oxygen edge. We used the optical depth at 21.7 Å, calculated from our best-fit model, and the corresponding cross-section at this wavelength ($\Delta\sigma = 4.2746 \times 10^{-19}$ cm² where $\Delta\sigma$ is the difference in cross-section from the top of the edge to the value at $\lambda = 21.7$ Å; Gorczyca & McLaughlin 2000) to determine the column density of oxygen (N_{O}). We estimate that this method has a systematic error of less than 5%. Away from the near-edge structure, the energy dependent cross-section of Gorczyca & McLaughlin (2000) matches the cross-section calculated by Verner & Yakovlev (1995). The Henke et al. (1993) cross-section is larger by $\approx 10\%$, resulting in smaller values of N_{O} and N_{H} when the Henke et al. (1993) cross-section is used for the same optical depth. It is also important to note that discrepancies in the inferred column densities may also arise when the cross-section at the ionization wavelength is used with an edge model placed at an arbitrary wavelength. Using the oxygen ISM abundance of Wilms et al. (2000), we calculated N_{H} . Table 3 gives the best fit values for the edge positions, depths and inferred column densities in the fixed continuum models. In addition, we give the difference in the calculated N_{O} between the fixed and free continuum models. These column densities do not include any correction for oxygen bound in dust grains or other molecules.

Table 4 lists the best-fit values of the line positions, widths, and EWs of the oxygen features in the fixed continuum method, in addition we show the difference in the EW as determined by the fixed and free continuum methods. The difference in EW is comparable to the statistical error on the measurements. Therefore, our fitting method should not greatly affect the results. The 23.51 Å line is accepted to be the $1s-2p$ transition of neutral oxygen. By combining the large number of sources in our sample, we find that the weighted mean value of the line position is 23.508 ± 0.003 Å. Figure 6 shows the position determinations of the O I line for the various datasets. Our sample includes one outlier, found in the Cyg X-1 ObsID 107 spectrum. An examination of the spectrum of this source (see Figure 3) suggests that the actual line position is higher, consistent with the other sources. The mean value of the O I line deviates by only 0.0005 Å when this observation is excluded from the sample.

Using our mean value for the O I absorption line as a benchmark, we can now shift all of the theoretical data to match, allowing us to compare with the other features in the oxygen edge region. The weighted mean position of the first edge is 22.836 ± 0.007 Å. This position is consistent with the $S = 3/2$ resonance series predicted at 22.76–22.84 Å. In addition, the lines with best-fit positions of 22.86–22.92 Å are reasonably consistent with the $1s-3p$ resonance line of the oxygen edge at 22.884 Å. With the resolution of the HETG, we should resolve the $1s-3p$, which must be in the spectra given the detection of the

TABLE 3. OXYGEN EDGE PARAMETERS

Source	λ (Å)	τ	N_{O} (10^{18} cm^{-2})	ΔN_{O} (10^{18} cm^{-2})	N_{H} (10^{21} cm^{-2})
Cyg X-2	22.821 \pm 0.013 22.631	0.55 \pm 0.11 <0.04	1.1 \pm 0.2	...	2.3 \pm 0.5
4U 1636–53	22.821 \pm 0.017 22.631	1.28 $^{+0.3}_{-0.17}$ <0.4	2.6 $^{+1.0}_{-0.3}$	–0.5	5.3 $^{+2.1}_{-0.7}$
4U 1820–30	22.82 \pm 0.07 22.631	0.65 \pm 0.07 <0.07	1.31 $^{+0.20}_{-0.14}$	–0.34	2.7 $^{+0.4}_{-0.3}$
4U 1735–44	22.832 22.631	1.1 \pm 0.4 0.6 \pm 0.4	3.4 \pm 1.2	–1.6	7 \pm 2
GX 9+9	22.86 \pm 0.02 22.631	1.1 \pm 0.3 <0.5	2.2 $^{+1.2}_{-0.6}$	–0.7	4.5 $^{+2.4}_{-1.2}$
4U 1543–624	22.832 22.631	1.4 \pm 0.6 <1.0	2.8 $^{+2.4}_{-1.2}$	+0.2	6 $^{+5}_{-2}$
Cyg X-1 ObsID 107	22.854 \pm 0.017 22.631	2.2 \pm 0.5 0.9 \pm 0.5	6.3 \pm 1.4	–0.7	13 \pm 3
Cyg X-1 ObsID 3407	22.838 \pm 0.013 22.631	0.70 \pm 0.10 0.48 \pm 0.11	2.4 \pm 0.3	+0.1	4.9 \pm 0.6
Cyg X-1 ObsID 3724	22.838 $^{+0.017}_{-0.07}$ 22.631	0.75 \pm 0.10 0.66 \pm 0.11	2.9 \pm 0.3	–0.3	5.8 \pm 0.6

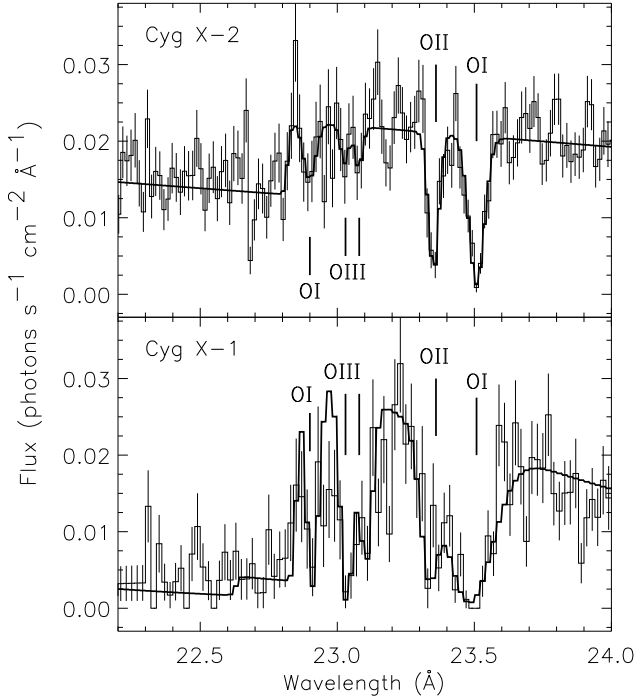


FIG. 3.— Flux spectra of the oxygen edge region for Cyg X-2 and Cyg X-1 ObsID 107. Line identifications are also shown.

$1s-2p$ line. We therefore identify the line at 22.88 Å as the $1s-3p$ resonance line from neutral oxygen absorption (see Figure 3 for identifications).

The combination of line EWs and column densities from the edges allows us to study the curve of growth of the neutral oxygen lines. A curve of growth describes the relationship between the line EW and the absorbing column density and can be separated into 3 regimes of column density dependence: linear, flat, and square-root. In the linear regime, the absorption line is not saturated

and the EW does not depend on the Doppler broadening of the line, yielding a linear dependence on the column density (N_{O}). As the line saturates with increasing N_{O} , the EW becomes explicitly dependent on the Doppler broadening as well as on the column density. This is known as the “flat part” of the curve of growth, where the EW is proportional to $(\ln N_{\text{O}})^{1/2}$. Finally, as the column density increases further, the Lorentzian wings of the line profile dominate. In this regime, the EW is proportional to $(N_{\text{O}})^{1/2}$. The flat part of the curve of growth is a powerful tool for studying the Doppler broadening of the absorbing material.

Using the cross-sections of Gorczyca & McLaughlin (2000), we have calculated the theoretical curve of growth for the $1s-2p$ and $1s-3p$ transitions of neutral oxygen with velocity dispersions of 20, 100, and 200 km s $^{-1}$ (Figure 7). Overlaid are the data from this analysis. Both the $1s-2p$ and $1s-3p$ measured EWs are consistent with the predicted values from the theoretical cross-sections, which corroborates our identifications for these lines. Our sample of X-ray binaries probes $N_{\text{O}}=10^{18}$ – 10^{19} cm^{-2} . For the $1s-2p$ transition (upper panel), this places us at the beginning of the $(N_{\text{O}})^{1/2}$ region of the curve of growth, where the contribution from Doppler broadening is less significant. There seems to be a systematic offset of the data from the expected values, which is possibly attributable to the use of a Gaussian function to fit the lines, instead of a Lorentzian or Voigt profile. The $1s-3p$ transition data points are a better match to the predicted values (lower panel). For this transition, we have moved fully into the flat region of the curve of growth. While the error in the data is comparable to the given spread in the curve of growth due to differences in the Doppler broadening, we can constrain the velocity dispersion of the ISM to $\lesssim 200 \text{ km s}^{-1}$.

For the line at ≈ 23.36 Å, our data give a weighted mean position of 23.351 ± 0.003 Å. Previous authors have attributed this line to the $1s-2p$ transition of neutral oxygen bound in compounds (Paerels et al. 2001; Schulz et al. 2002; Takei et al. 2002). However, recent calculations predict the O II $1s-2p$ absorption line at 23.33 Å

(Pradhan et al. 2003), and Kawatsura et al. (2002) measure the O II line at 23.35 Å. We therefore attribute this line to O II in the ISM (Figure 3).

Finally, we turn to the two absorption features in the 23.00–23.15 Å range. The weighted mean wavelengths of these features are 23.112 Å and 23.034 Å (with an error of 0.004 Å). As shown in Table 1, the positions of the O III lines are 22.99, 23.08, and 23.14 Å. The resolution of the MEG is high enough that these lines should be resolvable, but with the low countrates, we have binned the data 1.5–3 times the instrument resolution, which will cause the three lines to blend. Given that we are fitting three lines with two Gaussian absorption features, we would expect the measured positions to lie in between the predicted positions, which is what we found. As a test case, we fit one of the Cyg X-1 spectra (ObsID 3724) with three Gaussians for the O III region to determine if the lines could be reliably separated. When the wavelengths of the lines were fixed, significant detections of absorption lines at those positions were found. When the positions were free to vary, the lines were also significantly detected and with wavelengths consistent with the predictions of Pradhan et al. (2003), although with larger errors than found when only two lines were used to model the O III absorption. We therefore identify these absorption features with O III absorption (Figure 3).

We used the resonance oscillator strengths of Pradhan et al. (2003) to compute the curve of growth for the ionized oxygen lines. For O III, the total EW of the lines was used for comparison to the data. A curve of growth relates the EW and column density of a particular element and ionization state. We have not measured the column densities for ionized oxygen, instead, we compare the EW of the O II and O III lines to the column density of neutral oxygen. If we define the abundance $A = N_X/N_O$, where X is the ionization state under consideration, we can relate the column density of ionized oxygen to that of neutral oxygen. In Figure 8, we have plotted the curve of growth for O II (upper panel) and O III (lower panel) for three velocity dispersions (20, 100, and 200 km s⁻¹) and three abundances ($A=1.0$, 0.1, and 0.001). Both O II and O III are in the flat part of the curve of growth, making a determination of the abundance more difficult. For reasonable velocity dispersions ($\lesssim 200$ km s⁻¹), we can constrain the abundance of both ionization states. We find O II/O I ≈ 0.1 and O III/O I $\lesssim 0.1$.

It is interesting to note that the data points for O II show a large scatter. The two observations with the largest deviation are the most recent Cyg X-1 observations (ObsIDs 3407 and 3724), which are the most affected by the time-dependent instrumental contamination. Therefore, we suggest that the correction for the instrumental contamination may not be completely accurate in its fine structure, and care should be taken when drawing conclusions from the most recent data.

6. DISCUSSION

We have presented the first global study of oxygen K-shell absorption in the ISM. Using HETGS spectra of seven X-ray binaries, we have developed an empirical model consisting of 2 absorption edges and 5 absorption lines. The positions and strengths of the features were then compared to theoretical predictions for neutral and

ionized oxygen features. The neutral oxygen edge was resolved into the 1s-2p and 1s-3p transitions, while two edge models were used to describe the remaining, unresolved edge structure. From the curve of growth analysis, we constrain the velocity dispersion to $\lesssim 200$ km s⁻¹ for neutral oxygen in the ISM. We also detect several absorption features which we identify with the 1s-2p transitions of O II and O III. The ISM abundances for O II and O III, relative to O I, are found to be ≈ 0.1 and $\lesssim 0.1$, respectively. This is the first measurement of the O II/O I and O III/O I abundance of the ISM.

Our analysis relies on using the measured position of the neutral oxygen 1s-2p line as a benchmark with which to shift the theoretical wavelength predictions. Previous comparisons of theoretical predictions with laboratory data have shown good agreement of the line positions and strengths once a small overall wavelength offset ($\lesssim 50$ mÅ) is applied (McLaughlin & Kirby 1998; Gorczyca & McLaughlin 2000). This is at least partially due to systematic uncertainties in the absolute wavelength calibration of the laboratory data. Laboratory measurements of the 1s-2p transition of neutral oxygen range from 23.489 to 23.536 Å (see Stolte et al. 1997, and references therein) with quoted errors much less than the discrepancy among the measurements. In contrast, our results give a repeatable position for the 1s-2p transition (over all our sources) due to the HETGS's well-calibrated absolute wavelength scale. With a wavelength accuracy of 11 mÅ, our *Chandra* data is the best measurement of the absolute positions of these features. As an additional check, we can compare our results with the laboratory data for singly ionized oxygen. Kawatsura et al. (2002) measure the 1s-2p transition of O II at 23.35 Å, 0.08 Å greater than predicted by Pradhan et al. (2003) and consistent with our measured value. The laboratory data supports the need for shifts to the theoretical predictions.

6.1. Previous Results

Takei et al. (2002) fit the spectrum of Cyg X-2 with three edges in the oxygen K-shell region, two to represent the ²P and ⁴P edges found in atomic oxygen absorption and the other for oxygen in molecular compounds. The molecular edge had an edge wavelength of 23.13 Å, similar to the position found by Schulz et al. (2002) for the oxygen edge in Cyg X-1. This higher wavelength edge coincides with our identified O III absorption features, which could resemble an edge feature in lower resolution spectra. In the Cyg X-1 spectrum of Schulz et al. (2002), there is a significant count excess on the shorter wavelength side of the edge and at the time, this excess was attributed to either an instrumental effect or to emission lines from the source. Our model is more successful in fitting this structure (see Figure 3).

Other authors (Paerels et al. 2001; Schulz et al. 2002; Takei et al. 2002) have previously identified the O I 1s-2p line and the line at 23.35 Å in the spectra of X-ray binaries. The 23.35 Å line has been attributed to the 1s-2p transition in iron oxides based on the results of Wu et al. (1997) which suggest a narrow absorption feature at ≈ 23.3 Å. But in addition to the narrow absorption feature, there is a broad edge feature at ≈ 22.9 Å (Wu et al. 1997). In fact, given the relative cross-section

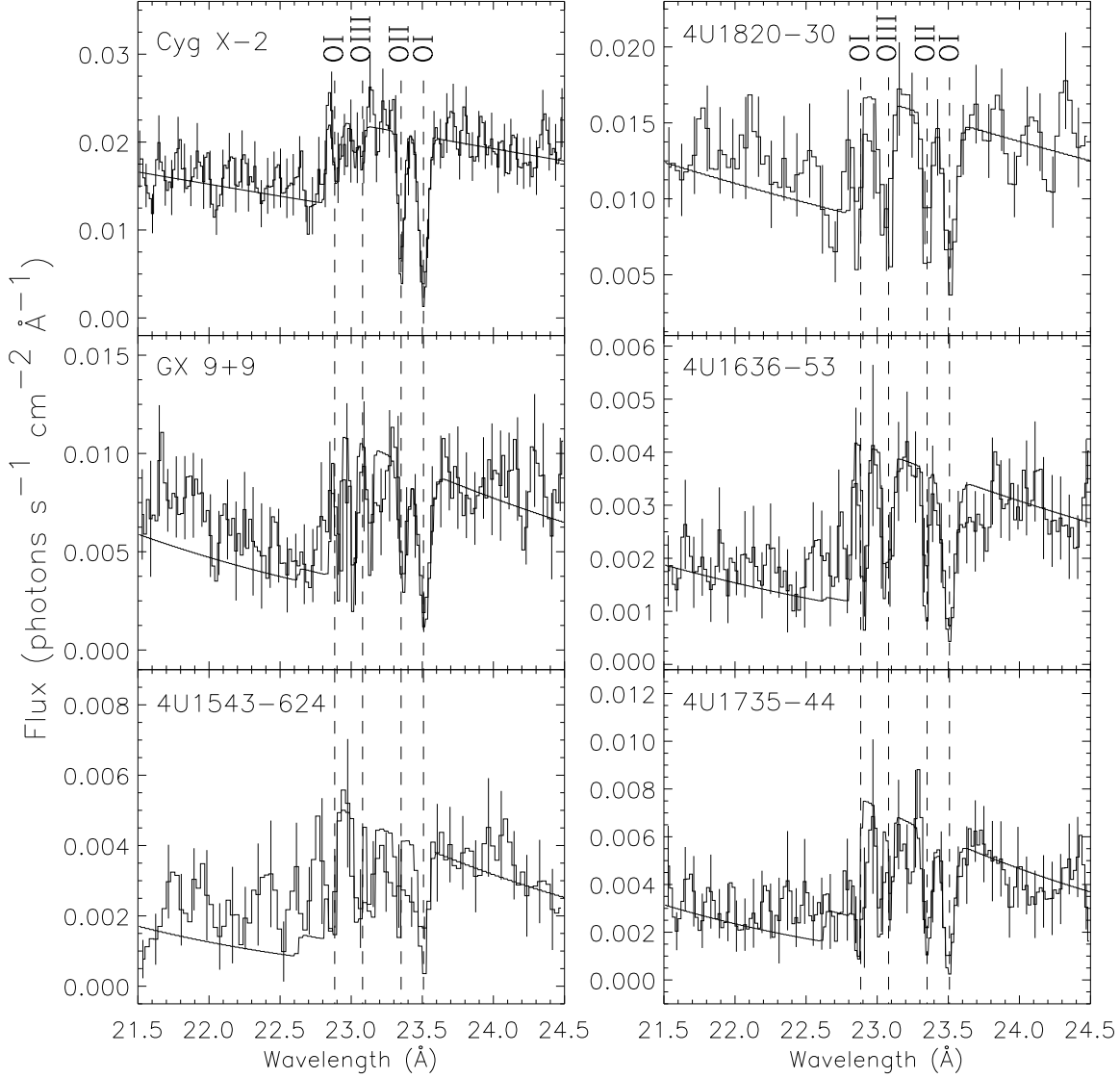


FIG. 4.— Flux spectra for six X-ray binaries included in this study. The best-fit model is also shown. The data have been smoothed for illustrative purposes and representative error bars are shown. The dashed lines indicate the positions of the identified features.

between the narrow line and the edge, the edge should be detectable before the line. This is opposite of the atomic oxygen cross-sections, where the narrow $1s-2p$ lines have larger cross-sections than the associated edges. This edge feature is not required by our data, which is fit well by just the neutral, atomic oxygen edge. Finally, the structure of molecular edges is dependent on the composition of the dust in the ISM, which is highly uncertain (Draine 2003). This, coupled with a lack of laboratory and theoretical results for molecular oxygen cross-sections, makes predicting the position and strength of molecular line features difficult.

We therefore attribute the 23.35 Å feature to absorption from O II since we expect ionized oxygen to be present in the ISM at the position we determined. In the warm, ionized phase of the ISM, the ionization of oxygen should track that of hydrogen due to a strong charge exchange process (Field & Steigman 1971).

Therefore we would expect that $N(\text{O II})/N(\text{O I}) \approx N(\text{H II})/N(\text{H I})$. Takei et al. (2002) estimate that for Cyg X-2, $N(\text{H II})/N(\text{H I}) = 0.32$. Reynolds (1991) found H II/H I of 0.2–0.6 along different lines-of-sight through the galaxy. Our estimate for $N(\text{O II})/N(\text{O I}) \approx 0.1$ is less than that found for hydrogen, but due to multiple electron ejections during photoionization (Watson & Kunz 1975), a more accurate comparison should be $[N(\text{O II}) + N(\text{O III})]/N(\text{O I})$. In either case, the presence of O II is expected at roughly the measured value, supporting our identification.

6.2. Contributions from Molecules and Dust?

Our data are well fit by our model which includes only neutral and ionized oxygen contributions. But the ISM should also contain oxygen in various compounds, including carbon monoxide (CO) and dust. In X-ray spectra, molecular forms of oxygen should produce a $1s-2p$ reso-

TABLE 4. OXYGEN LINE PARAMETERS

Source	λ (Å)	σ (Å)	EW (Å)	Δ EW (Å)
Cyg X-2	23.508 \pm 0.004	0.026 \pm 0.005	0.067 \pm 0.011	...
	23.352 \pm 0.005	0.016 \pm 0.007	0.041 \pm 0.011	...
	23.078 \pm 0.019	0.01	0.009 \pm 0.008	...
	23.03 \pm 0.03	0.01	<0.017	...
	22.899 $^{+0.06}_{-0.017}$	0.01	0.019 \pm 0.011	...
4U 1636–53	23.507 \pm 0.011	0.040 $^{+0.021}_{-0.014}$	0.09 \pm 0.03	-0.03
	23.340 \pm 0.008	<0.02	0.031 \pm 0.017	-0.003
	23.102 $^{+0.014}_{-0.06}$	0.01	0.020 \pm 0.010	-0.005
	23.056 \pm 0.013	0.01	0.027 \pm 0.010	-0.004
	22.915 \pm 0.013	0.01	0.034 \pm 0.010	-0.004
4U 1820–30	23.514 \pm 0.010	0.034 \pm 0.015	0.07 \pm 0.02	-0.02
	23.351 \pm 0.014	<0.04	0.04 \pm 0.02	-0.01
	23.086 \pm 0.017	0.01	0.033 \pm 0.013	-0.004
	23.03 \pm 0.06	0.01	0.023 \pm 0.013	-0.004
	22.867 \pm 0.015	0.01	0.036 \pm 0.016	-0.004
4U 1735–44	23.503 \pm 0.009	0.033 \pm 0.015	0.08 \pm 0.03	-0.02
	23.354 \pm 0.017	0.027 \pm 0.014	0.06 \pm 0.02	-0.03
	23.095 \pm 0.017	0.01	0.027 \pm 0.013	-0.016
	23.020 \pm 0.007	0.01	0.036 \pm 0.009	-0.010
	22.861 \pm 0.006	0.01	0.040 \pm 0.009	-0.008
GX 9+9	23.517 \pm 0.009	0.036 \pm 0.016	0.08 \pm 0.03	-0.02
	23.367 \pm 0.017	0.026 \pm 0.014	0.050 \pm 0.019	-0.018
	23.133 \pm 0.010	0.01	0.024 \pm 0.010	-0.007
	23.017 \pm 0.011	0.01	0.034 \pm 0.010	-0.006
	22.906 \pm 0.018	0.01	0.031 \pm 0.011	-0.006
4U 1543–624	23.507 \pm 0.011	0.025	0.068 \pm 0.011	-0.005
	23.33	0.01	0.026 \pm 0.017	-0.009
	23.141 \pm 0.010	0.01	0.035 \pm 0.015	-0.012
	23.050 \pm 0.011	0.01	0.038 \pm 0.015	-0.010
	22.871 \pm 0.008	0.01	0.043 \pm 0.015	-0.009
Cyg X-1	23.482 \pm 0.019	0.086 $^{+0.014}_{-0.02}$	0.21 \pm 0.06	-0.06
ObsID 107	23.333 \pm 0.015	<0.05	0.05 $^{+0.05}_{-0.03}$	-0.001
	23.106 \pm 0.017	0.01	0.044 \pm 0.011	-0.009
	23.036 \pm 0.009	0.01	0.056 \pm 0.006	-0.002
	22.910 \pm 0.013	0.01	0.053 \pm 0.011	-0.008
Cyg X-1	23.518 \pm 0.009	0.061 \pm 0.017	0.095 \pm 0.017	-0.018
ObsID 3407	23.370 \pm 0.012	0.019 $^{+0.018}_{-0.011}$	0.020 \pm 0.011	-0.001
	23.092 \pm 0.009	0.01	0.018 \pm 0.005	-0.001
	23.044 \pm 0.010	0.01	0.017 \pm 0.006	-0.002
	22.885 \pm 0.017	0.01	0.011 \pm 0.006	-0.002
Cyg X-1	23.505 \pm 0.006	0.05	0.094 \pm 0.007	-0.005
ObsID 3724	23.349 \pm 0.010	0.01	0.009 \pm 0.005	-0.007
	23.118 \pm 0.010	0.01	0.030 \pm 0.006	-0.007
	23.039 \pm 0.018	0.01	0.024 \pm 0.006	-0.007
	22.870 $^{+0.04}_{-0.018}$	0.01	0.022 \pm 0.014	-0.006

nance feature at a wavelength shifted from that of atomic oxygen due to the effects of the bonds on the electron energy levels. We recognize that there are unidentified features in the spectra with strengths comparable to some of the smallest EW features we identify. It is possible that these features could be attributable to molecular features, though any quantitative statements depend on predictions or measurements of the strength and positions of these features, which are unavailable at this time.

Although our data do not require such contributions, we can estimate an upper limit to the amount allowed by our data. If we take the error estimate for our measured column densities to be the upper limit on the amount of oxygen bound in molecules, and assuming the cross-section for molecular oxygen is comparable to that for atomic, then 10–40% of the oxygen can be bound and still not be detected. A similar limit can be placed if we identify the 23.35 Å feature as due to a molecular contribution as has been previously suggested (Paerels et al.

2001; Schulz et al. 2002; Takei et al. 2002). In this case, the ratio of molecular to atomic oxygen would be roughly the same as we suggest for O II/O I, $\approx 10\%$. This assumes that the oscillator strength for molecular oxygen, which is unknown, is similar to that of O II. These estimates compare well with the expected amount from other studies. André et al. (2003) calculated that the theoretical maximum amount of oxygen which can be found in dust grains is $(\text{O}/\text{H})_{\text{dust}} \leq 180$ ppm by comparing the ISM abundance of oxygen to magnesium, silicon, and iron. Given the measured oxygen abundances in the ISM and the Sun, they found an average for $(\text{O}/\text{H})_{\text{dust}} = 109$ ppm, which translates to 27% of the oxygen in the ISM. André et al. (2003) also found that the amount of oxygen bound in grains varied between lines of sight, from 1–40%. Higher signal-to-noise spectra will be required to measure the effect of dust and molecules on the oxygen edge in X-ray spectra.

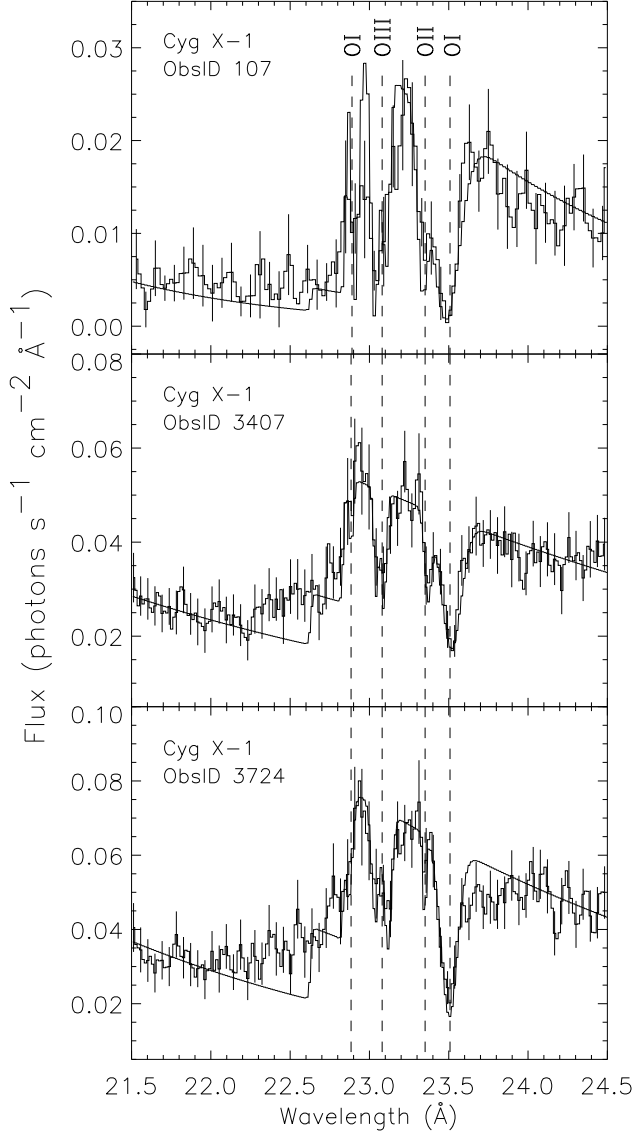


FIG. 5.— Flux spectra and best-fit model for the three Cyg X-1 observations. The data have been smoothed for illustrative purposes and representative error bars are shown. The dashed lines indicate the positions of the identified features. Note the reduction in the relative strength of the O II to O I absorption lines (23.35 and 23.51 Å, respectively). We attribute this to possible problems in the modeling of the time-dependent contaminant.

6.3. Alternatives to Interstellar Origin

Although we have attributed the identified features to interstellar oxygen absorption, we also consider alternative explanations for completeness. Pre-launch studies of the instrumental oxygen absorption features do not show any significant features that would account for the absorption lines we have found, other than the 23.33 Å absorption line from the OBF (Prigozhin et al. 1997). In addition, the correlation of the line EWs with neutral column density would not be seen from an instrumental feature. Instrumental features would be expected to give the same EW regardless of the source and would be seen in observations of all sources, including low column

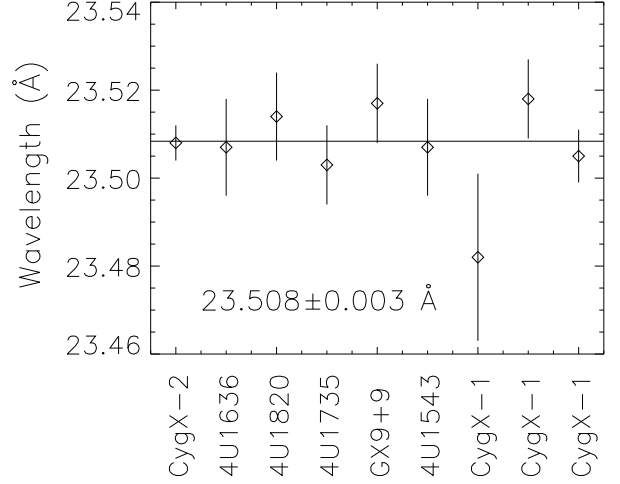


FIG. 6.— Best fit position of the $1s-2p$ absorption line from O I. The weighted mean value of the line position is given. The outlier is from the Cyg X-1 ObsID 107 data. All quoted errors are statistical errors only and do not include the instrumental wavelength error of ± 0.011 Å (FWHM).

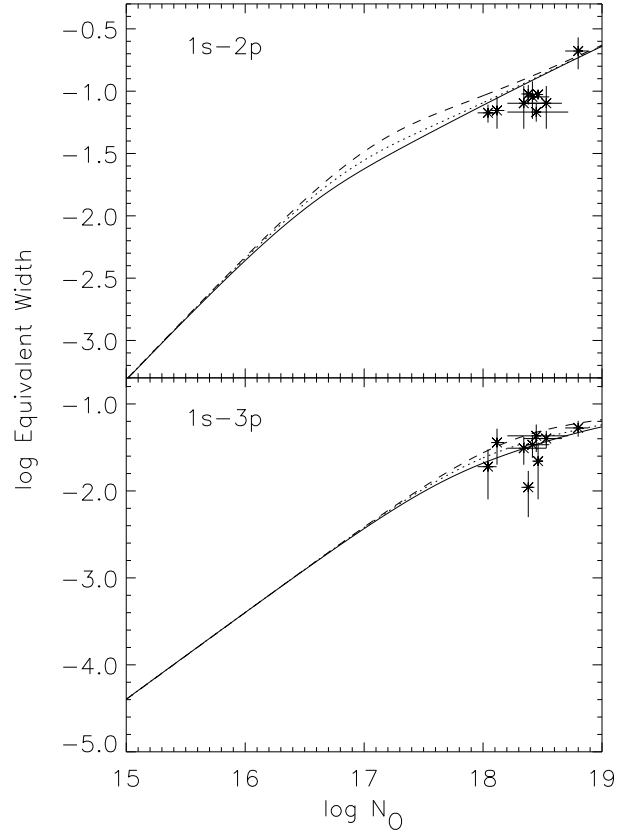


FIG. 7.— Curve of growth for the $1s-2p$ and $1s-3p$ transitions of neutral oxygen. The solid, dashed, and dotted lines indicate the predicted EWs for velocity dispersions of 20, 100, and 200 km s⁻¹, respectively.

density extragalactic sources, like those used for calibration of the contaminant contribution. We know of no identification of these features in lower column sources. Therefore, we reject an instrumental origin for our detected line features.

That being said, there does seem to be some effect on the EW determinations of the O II line from the time-dependent contaminant absorption. For most of our data, the contaminant effect is small and does not impact our results for the ISM. The most recent observations however, which would have the largest contaminant correction, have lower EWs than predicted from the curve of growth of the other data points. One possible explanation is that there is a non-negligible O II absorption line in the spectra of the calibration source. We note that the structure of the oxygen contaminant absorption is primarily taken from a single observation (Marshall et al. 2003). By not accounting for ISM O II, the contaminant correction is larger than necessary, reducing our measured EWs, particularly as the correction grows larger. It is hoped that our study can help the calibration team understand ISM contributions to the oxygen edge region in order to more accurately model the contaminant. Additionally, the most recent observations of Cyg X-1 also show an excess of counts in the 22.2–22.6 Å range. Since these are the only observations with this feature, it is again possible that it is due to the effect of the contaminant or the contaminant model.

Accepting that the line features are from ionized oxygen species, we must ask the question are these features truly from the ISM, or rather do they originate in material local to the X-ray binaries. The continuum emission from the binaries provide a great source of ionizing radiation, which could create ionization bubbles around the systems. The amount of ionized oxygen found in each system would depend on the luminosity of the X-ray source, and the density and composition of material surrounding the source. To first order, if the density of material is taken to be similar for all systems, the more luminous systems will be able to ionize more oxygen and would then be expected to have the largest measured EWs. Of our sources, Cyg X-1 and Cyg X-2 are the most luminous, yet Cyg X-2 has some of the smallest measured EWs. This is expected if the ionized material is interstellar, since Cyg X-2 also has the smallest neutral oxygen column density from the edge determination. While the O II data points do not show a significant trend with column density, most likely due to problems with modeling of the contaminant as mentioned previously, the EWs of O III are correlated with the neutral oxygen column density. Given that the sources included in our sample span more than two orders of magnitude in luminosity and several orders of magnitude in orbital separation, it is highly unlikely that the correlation between the O III EW and the neutral column density could be produced by absorption from material local to the binaries. On the other hand, the correlation is exactly what is expected if all of the absorption features are interstellar in origin.

Along with the lower ionization species found here, we would expect the binaries to produce absorption features from more highly ionized forms of oxygen. Of our sources, only Cyg X-1 has shown other absorption features (Schulz et al. 2002; Feng et al. 2003; Miller et al.

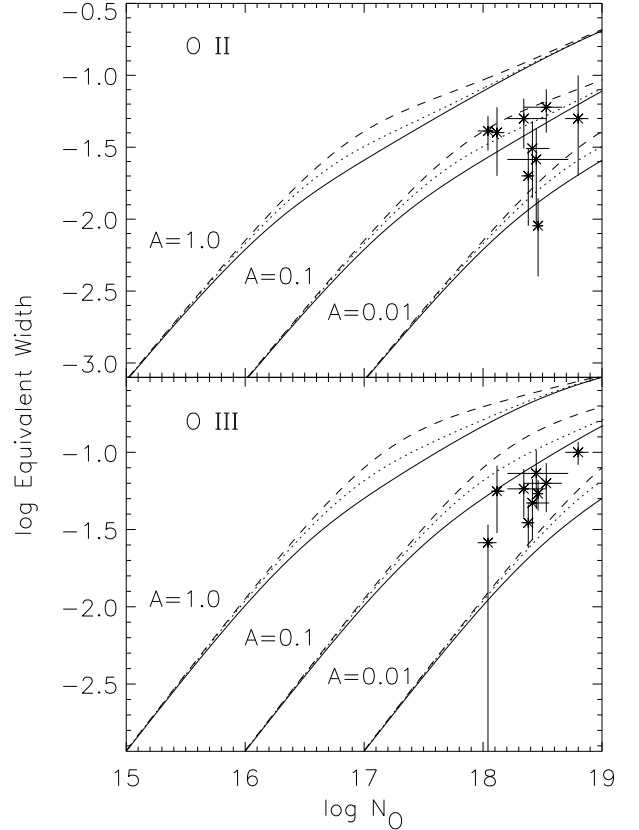


FIG. 8.— Curve of growth for the O II and O III absorption features. The O III EW is the total EW from the multiple absorption lines. The solid, dashed, and dotted lines indicate the predicted EWs for velocity dispersions of 20, 100, and 200 km s^{−1}, respectively. Also included are predicted EWs for various abundances ($A = N_X/N_O$) relative to neutral oxygen.

2003), and it is the only source with multiple observations that can be used to study variations of the column densities. In the three observations of Cyg X-1, we measure a change of the neutral oxygen column density of a factor of 2, which seems unreasonably high for variations in the ISM. Cyg X-1 is a high-mass X-ray binary system that accretes from the stellar wind of the young, massive companion. This, combined with the detection of other more highly ionized absorption lines, points to local material in this system. If the fluxes of the observations are compared, we find that ObsID 107 has the lowest continuum flux at the oxygen edge region and the highest neutral column density. The fluxes are larger in ObsIDs 3407 and 3724 with smaller columns. We postulate that as the flux of Cyg X-1 increases, so does the ionization of the local material (but see Wen et al. 1999; Feng et al. 2003, for a discussion of the dependence on orbital phase). In ObsIDs 3407 and 3724, the local material is most likely highly ionized, removing any local contributions to the neutral and low ionization features. Measurements of the other absorption lines may help to verify this hypothesis.

This paper represents the first in a series of studies of the properties of the ISM using high-resolution X-ray spectra. Future work will include studies of lower column

density sources to map out the curve of growth of the different oxygen absorption lines. More data will allow us to better constrain the velocity dispersion and ionization fraction of the oxygen in the ISM. Additionally, we will perform a similar analysis on the other astrophysically abundant elements, which can be used to study abundances and depletion in the ISM. Studies of the ISM in X-rays provides a unique opportunity to measure a large variety of elements and ionization states.

Some interesting questions that will be addressed in the future are the relationship between the warm, neutral (WNM) and warm, ionized (WIM) phases of the ISM and the source of the ionizing flux. From an ultraviolet observation of the Galactic halo star HD 93521, Spitzer & Fitzpatrick (1993) found that the WIM coincided with the WNM. Other studies (Howk & Savage 1999; Reynolds et al. 1995) have found similar results. It has been suggested that the ultraviolet flux from O stars would provide enough energy to produce the WIM

(see Heiles & Kulkarni 1987). However, the ionization fraction of helium found by Reynolds & Tufté (1995) is much lower than expected for the O star ionization models. New observations from the *Far Ultraviolet Spectroscopic Explorer* and the Wisconsin H-Alpha Mapper will help to resolve this issue. In addition, the high-resolution X-ray spectra available from *Chandra* and *XMM* will provide information on the ionization fraction of heavier elements in the ISM, providing more data from which to understand the source of the ionizing radiation.

We thank Claude Canizares, Carl Heiles, Frits Paerels, and Ken Sembach for useful discussions and comments. We would also like to thank Tom Gorczyca for providing us with the neutral oxygen cross-section calculation and for comments on the manuscript. This work was supported in part by NASA under contracts NAS8-01129 and grant NAG5-9184.

REFERENCES

- André, M. K., et al. 2003, *ApJ*, 591, 1000
 Bałucińska-Church, M. & McCammon, D. 1992, *ApJ*, 400, 699
 Bautista, M. A. 2000, in *Atomic Data Needs for X-ray Astronomy*, ed. M. A. Bautista, T. R. Kallman, A. K. Pradhan, 25 (<http://heasarc.gsfc.nasa.gov/docs/heasarc/atomic/>)
 Brown, R. L. & Gould, R. J. 1970, *Phys. Rev. D*, 1, 2252
 de Vries, C. P., den Herder, J. W., Kaastra, J. S., Paerels, F. B., den Boggende, A. J., Rasmussen, A. P. 2003, *A&A*, 404, 959
 Draine, B. T. 2003, *ARA&A*, 41, 241
 Feng, Y. X., Tennant, A. F., & Zhang, S. N. 2003, *ApJ*, 597, 1017
 Field, G. B. & Steigman, G. 1971, *ApJ*, 166, 59
 Gorczyca, T. W. & McLaughlin, B. M. 2000, *Journal of Physics B: Atomic, Molecular, and Optical Physics*, 33, 2000
 Heiles, C., & Kulkarni, S. R. 1987, in *Physical Processes in Interstellar Clouds*, ed. G. E. Morfill & M. Scholer (Dordrecht: Reidel), 13
 Henke, B. L., Gullikson, E. M., & Davis, J. C. 1993, *Atomic Data & Nucl. Data Tables*, 54, 181
 Howk, J. C. & Savage, B. D. 1999, *ApJ*, 517, 746
 Kawatsura, K., et al. 2002, *Journal of Physics B: Atomic, Molecular, and Optical Physics*, 35, 4147
 Marshall, H. L., Tennant, A., Grant, C. E., Hitchcock, A. P., O'Dell, S., & Plucinsky, P. P. 2003, in *X-Ray and Gamma-Ray Instrumentation for Astronomy XIII*, ed. K. A. Flanagan & O. H. Siegmund, SPIE Conf. Proc., 5165, 497
 McLaughlin, B. M. & Kirby, K. P. 1998, *Journal of Physics B: Atomic, Molecular, and Optical Physics*, 31, 4991
 Menzel, A., Benzaid, S., Krause, M., Caldwell, C. D., Hergenbahn, U., & Bissen, M. 1996, *Phys. Rev. A*, 54, R991
 Miller, J. M., et al. 2003, *ApJ*, submitted, (astro-ph/0208463)
 Morrison, R. & McCammon, D. 1983, *ApJ*, 270, 119
 Paerels, F., et al. 2001, *ApJ*, 546, 338
 Pradhan, A. K., Chen, G. X., Delahaye, F., Nahar, S. N., & Oelgoetz, J. 2003, *MNRAS*, 341, 1268
 Prigozhin, G. et al. 1997, *IEEE Transactions on Nuclear Science*, 44, 970
 Reynolds, R. J. 1991, in *IAU Symp. 144, in The Interstellar Disk-Halo Connection in Galaxies*, ed. H. Bloemen (Dordrecht:Kluwer), 67
 Reynolds, R. J. & Tufté, S. L. 1995, *ApJ*, 439, L17
 Reynolds, R. J., Tufté, S. L., Kung, D. T., McCullough, P. R., & Heiles, C. 1995, *ApJ*, 448, 715
 Ride, S. K. & Walker, A. B. C. 1977, *A&A*, 61, 339
 Schattenburg, M. L. & Canizares, C. R. 1986, *ApJ*, 301, 759
 Schulz, N. S., Cui, W., Canizares, C. R., Marshall, H. L., Lee, J. C., Miller, J. M., & Lewin, W. H. G. 2002, *ApJ*, 565, 1141
 Spitzer, L. & Fitzpatrick, E. L. 1993, *ApJ*, 409, 299
 Stolte, W. C., et al. 1997, *Journal of Physics B: Atomic, Molecular, and Optical Physics*, 30, 4489
 Takei, Y., Fujimoto, R., Mitsuda, K., & Onaka, T. 2002, *ApJ*, 581, 307
 Verner, D. A., Yakovlev, D. G., Band, I. M., & Trzhaskovskaya, M. B. 1993, *Atomic Data & Nucl. Data Tables*, 55, 233
 Verner, D. A. & Yakovlev, D. G. 1995, *A&AS*, 109, 125
 Watson, W. D. & Kunz, A. B. 1975, *ApJ*, 201, 165
 Weisskopf, M. C., Brinkman, B., Canizares, C., Garmire, G., Murray, S., & van Speybroeck, L. P. 2002, *PASP*, 114, 1
 Wen, L., Cui, W., Levine, A. M., & Bradt, H. V. 1999, *ApJ*, 525, 968
 Wilms, J., Allen, A., & McCray, R. 2000, *ApJ*, 542, 914
 Wu, Z. Y., Gota, S., Jollet, F., Pollak, M., Gautier-Soyer, M., & Natoli, C. R. 1997, *Phys. Rev. B*, 55, 2570